Novel correlations between process forces and void morphology for effective detection and minimization of defects during friction stir welding

Mohammad Ali Ansari¹, Hemant Agiwal², Mike Zinn³, Frank Pfefferkorn⁴, Shiva Rudraraju^{5,*}

- 1 Department of Mechanical Engineering, University of Wisconsin-Madison, USA, email: mansari3@wisc.edu
- 2 Department of Mechanical Engineering, University of Wisconsin-Madison, USA, email: agiwal@wisc.edu
- 3 Department of Mechanical Engineering, University of Wisconsin-Madison, USA, email: mike.zinn@wisc.edu
- 4 Department of Mechanical Engineering, University of Wisconsin-Madison, USA, email: frank.pfefferkorn@wisc.edu
- 5 Department of Mechanical Engineering, University of Wisconsin-Madison, USA, email: shiva.rudraraju@wisc.edu

 * Corresponding Author, email: shiva.rudraraju@wisc.edu

Abstract

Sub-surface defects and material heterogeneities resulting from the friction stir welding (FSW) process have, to a certain degree, limited the wider industrial adoption of this solid-state welding process. However, in-process defect detection techniques for measuring welding quality have the potential to replace expensive and time-consuming post-process inspection of defects. Current in-process defect detection techniques rely on approaches that try to directly correlate the part-scale welding quality to defect formation, without a fundamental understanding of the underlying mechanics and materials physics that modulate defect evolution. In this work, we demonstrate an effective in-process numerical technique that uses process force signals to detect volumetric void formation and connect the variations in the force signals to interactions between the tool probe and the underlying material voids. Our approach relies on a highfidelity Finite Element Analysis (FEA) simulation of the FSW process, and on correlation of numerically obtained process force signals with the corresponding void structures. This correlation is obtained in the phase-space relating in-plane reaction forces on the tool to the tool rotation angle. We focus on the interactions of the tool geometry and tool motion with the surrounding material undergoing plastic deformation and deduce novel insights into various correlations of tool motion and void formation. Through this approach, we can identify tool-related process conditions that can be optimized to minimize void formation and demonstrate a potential in-situ force-based void monitoring method that links to the underlying plastic flow and defect structures during the FSW process.

Keywords: Aluminum alloys, finite element analysis, defect formation, voids, friction stir welding, material flow, plasticity

1. Introduction

Friction stir welding (FSW) is a solid-state welding technique invented by The Welding Institute (TWI) in 1991 [1]. With process temperatures below solidus, FSW avoids fusion-related defects such as hot cracking, spattering, etc., and thus improving the weld quality in comparison to traditional fusion welding processes. FSW also permits the joining of difficult welds and dissimilar alloys [2-4]. Further, no requirement of any filler material, absence of fumes, and elimination of shielding gas ensures that FSW has a lower environmental impact. The fundamental mechanics underlying the process is the intense plastic deformation due to high strain rates that lead to material fusion and dynamic recrystallization in the stir zone. These characteristics, combined with lower residual thermal effects, make FSW an energy-efficient method of creating high-quality joints for many widely used engineering metallic materials like Aluminum alloys, Magnesium alloys, and Stainless Steel [3]. However, sub-surface defects and material heterogeneities resulting from the FSW process have, to a certain degree, limited the wider industrial adoption of this solid-state welding process. In-process defect detection techniques that are based on measuring welding quality have the potential to replace some expensive and time-consuming post-process

inspection of defects. Current in-process defect detection techniques rely on approaches that try to directly correlate the part-scale welding quality to defect formation, without a fundamental understanding of the underlying mechanics and materials physics that modulate defect evolution.

In this work, we seek to demonstrate an in-process numerical technique that uses process force signals to detect volumetric void formation and connect the variations in the force signals to interactions between the tool probe and the underlying material voids. This work is a continuation of the FSW experimental studies performed by our group in Franke et al. [31], which indicated that volumetric voids formed with tools, including three flats on the probe, distort the oscillatory component of the process force signal. The oscillatory process force signal at the tool rotational frequency was described by identifying the opening and filling of a cavity in the wake of the tool probe. However, a comprehensive correlation of the probe-void interactions and various distortions of the oscillatory component of the process force signal cannot be established with limited experimental data. In this work, a Finite Element method based numerical approach for modeling FSW was developed for identifying and characterizing the process forces and their correlation with the underlying material flow and defect (void) structures. This model is employed to numerically extract the process force signals and the corresponding volumetric void distributions in the vicinity of the probe. We focus on the interactions of the tool geometry and tool motion with the surrounding material undergoing plastic deformation and deduce novel insights into various correlations of tool motion and void formation. Through this approach, we demonstrate that we can identify tool-related process conditions that can be optimized to minimize void formation. This can potentially lead to the development of an in-situ force-based void monitoring method that links to the underlying material plastic flow during the FSW process.

In the following subsections of this introduction, we provide a literature survey of the state of material flow modeling, in-situ monitoring of voids, and related numerical approaches that are popular in modeling of FSW. Beyond the introduction, we present the experimental and numerical methods used in this work, followed by a detailed description of the results and their discussion.

1.1. Intermittent material flow during FSW

Extensive research has been published hypothesizing various mechanisms to understand the material flow and mechanics underlying FSW. Cross-sectional imaging has regularly revealed an extruded band of material in the horizontal plane of the FSW setup. This intermittence is also observed in the tool force signals recorded during the process. The origins of oscillatory force signal and the intermittent banded structure were first discussed by Arbegast [5] and then expanded upon by Boldsaikhan et al. [6]. These authors hypothesized periodic cavity opening and filling around the tool probe with each tool revolution. Zaeh and Gebhard [7] investigated the material transport around the tool by the periodic action of the tool. Material transportation around the tool happened by the interaction of tool probe and workpiece material which causes intermittent material flow. Variation in shear bands by measuring a single band was measured by Fonda et al. [8] which led them to propose that the oscillatory motion of the tool because of the tool eccentricity (runout) or deflection causes weld banded structure. The intermittency has also been attributed to multiple process dynamics such as the stick-slip friction condition between tool and workpiece [9], tool runout [10], and probe features [11, 12]. Overall, developing an understanding of the physics underlying defect formation has been one of the centerpieces of research in the FSW scientific community. Intermittent material flow is critical to bolster this understanding, and recent studies have investigated the role of insufficient plastic flow within the periodic motion of the tool to volumetric sub-surface defects [13, 14].

1.2. In-process monitoring for void detection in FSW

One of the most discussed limitations of FSW is the cost of investigating sub-surface defects. Nondestructive evaluation (NDE) methods such as eddy current testing [15] and ultrasonic testing [16, 17]

have been explored in the past, however, the cost and time involved with these methods are significant and this often acts as a dampener to their extensive adoption in the context of FSW. If one assumes that the oscillatory property of the tool reaction force signal is directly linked to the plastic flow of material around the probe, then a breakdown in the material plastic flow would result in a distortion of this process force signal. Over the years, various researchers have suggested in-situ volumetric void detection methods as alternates to expensive post-process inspections, and as a mechanism to enable accurate in-process corrective action. Along these lines, if distortion in the process forces signal can be captured and correlated to the occurrence of volumetric voids, the need for costly inspections can be eliminated and replaced with accurate in-process monitoring. Mishra et al. [18] have shown in-process monitoring and process control in FSW by mainly focusing on force and torque measurements. Several different techniques based on process force and torque signals have been discussed in the literature [19-24]. One general observation that can be made about existing literature on this topic is that most prior studies do not tease out a fundamental understanding of what is physically happening during the process and what creates the distortion in forces/torques signals at the time of void formation. More recently, the use of machine-learning algorithms combined with frequency analysis of force signals to link distortions in the measured signals to the occurrence of voids is gaining popularity, including some of our recent work [31]. While these techniques are important black-box approaches, they are limited by the need for extensive training of the algorithms with experimental data that is often sparse, and limiting the in-process monitoring technique to the vicinity of the solution space of known process variations such as probe geometry, welding machine stiffness, workpiece material, etc. Currently, there is an absence of a fundamental understanding of what is happening within the measured force signal under process conditions leading to volumetric void formation, and a lack of understanding of the correlation between force signal variations and the underlying plastic flow and defect structures. This current study seeks to address this limitation and is discussed in detail in the subsequent sections.

1.3. Computational methods for void detection and material flow analyses

Existing research has strongly demonstrated that numerical modeling is a powerful tool in terms of gaining a fundamental understanding of the material plastic flow inherent to FSW. Some of the relevant computational studies are listed below.

To model the material flow and predict deformation during the FSW process, the numerical methods of choice are computational fluid mechanics (CFD) and computational solid mechanics (CSM). Depending on the intensity of the plastic flow that needs to be modeled one chooses a CFD (Eulerian approach) or CSM (Lagrangian approach) based technique. However, recent computational mechanics frameworks like Arbitrary Lagrangian-Eulerian (ALE) or Coupled Eulerian-Lagrangian (CEL) formulations try to bring the best of both worlds together, and are widely used to predict plastic flow and volumetric void formation.

Schmidt and Hattel [25] simulated the plasticized nugget zone and weld voids using the ALE framework. To avoid the high computational cost of the ALE formulations and the incapability of CFD frameworks towards predicting plasticity and void formation, the CEL framework is being widely used in recent literature, and hence is also adopted in this current study. CEL enables better modeling of the material flow, formation of plasticized nugget zone, and different types of voids that might occur during FSW. Al-Badour et al. [26] developed a CEL formulation to explore the effect of coefficient of friction and process parameters on weld quality and void formation. Zhu et al. [27] have used the same framework to investigate the probe geometry and its effect on material flow during FSW. They showed that the probe feature has a substantial impact on weld quality. Dialami et al. [28, 29] created a numerical framework based on ALE and CEL stages, and by adding a particle tracing strategy, this framework could simulate defects like joint line remnants. Ajri et al. [30] have simulated different voids including cavity, tunnel, groove-like, and

excess flash formation using the CEL framework. Further, the dependence of void formation on temperature distribution, equivalent plastic strain, and material flow were investigated using this model.

The objective of this study is using a high-fidelity finite element modeling framework to gain a fundamental understanding of the correlation between the process forces and the underlying void structures. In the context of intermittent material flow, we show that the resultant interaction force is due to an eccentric motion of the tool in the workpiece material. The interaction of probe features and the workpiece material leads to the intermittent material flow that in turn causes oscillatory force signals.

2. Materials and Methods

2.1. Experimental procedure

In this study, friction stir welding was performed by a 3-axis CNC milling machine (HAAS TM-1). A three-axis piezo-electric force dynamometer (Kistler, model 9265) was used to measure the forces applied to the workpiece by the tool in a three-axis coordinate system defined by the axis of the tool (Z), the direction of travel (Y), and perpendicular to travel in the plane of the workpiece surface (X). Signals from the dynamometer were guided to the charge amplifiers to read the forces by the DAQ system (National Instruments, BNC-2090A, PCI-6014, PCIe-6320). The average steady-state forces during the stirring phase are the only force that is analyzed in this study. The Friction Stir tool was made of hardened H13 tool steel consisting of a 15 mm diameter concave shoulder and a threaded probe that tapered from 7 mm to 5mm in diameter with three 0.635 mm deep flats. Toolholder resulted in a natural true runout for the tool equal to 64 µm, when it's rotating freely in the spindle and measured by a dial indicator at the tool shoulder. The origin of the tool runout is due to the tool and holder manufacturing process [31]. All workpieces were made of 6061-T6 aluminum alloys with approximate dimensions of $200 \times 100 \times 6$ {mm} 3 . All 120 mm long friction stir welding tests were performed with a 3° travel angle, using a mild steel backing plate with a thickness of 6.35 mm. The stiffness of the milling machine plus the tool and tool holder in the direction of interest (X and Y directions) was measured by the small incremental movement of the machine table in both directions to maintain contact between the friction stir tool and the dynamometer fixture. The force data is recorded by the dynamometer while the tool deflection was measured by a dial indicator that was fixed to an isolated static structure. The measured stiffness of the system in X and Y directions are 6150 kN/m and 8300 kN/m respectively.

To get a consistent plunging depth for all tests, a defined preload was used by the gage block at the trailing edge of the tool shoulder and the workpiece. The plunging phase was achieved by applying a constant plunging speed of 25 mm/min and a shoulder plunging depth of 0.2 mm. After the plunging phase, dwelling time was set at 0.2 s to increase the temperature by rotating the tool at its place, and then the tool was moved in the traverse direction with a 3-degree travel angle and constant speed. Table 1 shows all the experimental details of the current study. All tests were performed on a single block of Aluminum and in the extrusion-direction of the plates while the initial temperature was equal to the surrounding temperature (25 °C). Each experiment for a given set of parameters was performed three times to establish repeatability.

Table 1. Experimental details

Workpiece material	6061-T6 Aluminum
Workpiece dimensions	200 x 100 x 6 mm
Backing plate material	Mild steel
Travel angle	3°
Work angle	0°
Commanded Plunge depth	0.2 mm
Weld length	120 mm
FS Tool material	H13 tool steel

FS Tool shoulder: concave angle
FS Tool shoulder: diameter
FS Tool probe: major diameter
FS Tool probe: minor diameter
FS Tool probe: length
FS Tool probe: thread pitch
Rotational speed (rpm)
Traverse speed (mm/min)

3°
7 mm
7 mm
5 mm
15 mm
15 mm
1.588 mm
1000
200, 600

Post welding, each weld was sectioned perpendicular to the welding traverse direction to investigate the stirred zone area. Three transverse cross-sections (around 15 mm apart from each other) were cut to ensure that the weld reached the steady-state condition in terms of the forces and defect morphology. Cross-sections of the welding samples were ground, polished, and etched in a Poulton's reagent with extra HNO3 with an etching time of 10-20 s, so as to illuminate any sub-surface defects using white light optical microscopy (Alicona Infinite Focus).

2.2. Numerical Modeling

To model the FSW process and the associated material deformation, contact mechanics and thermomechanics, the Coupled Eulerian-Lagrangian (CEL) framework available within the ABAQUS [32] Explicit Finite Element package was adopted. The details about the CEL framework, material model (Johnson-Cook model), frictional contact model, and modeling assumptions and boundary conditions have been presented in an earlier publication by the authors [33]. The specific goal of the current research is to use this numerical framework to extract and examine the reaction force between the probe and workpiece, and to correlate the force variations with the underlying sub-surface defect morphology (absence or presence of volumetric voids and their morphology). The 3D numerical model geometry, material properties, and boundary conditions were chosen to closely model the experimental setup and conditions described in Section 2.1. In addition to the usual material properties of the workpiece, measured properties (tool runout and system setup stiffness described in Section 2.1) characteristic of the FSW setup were also incorporated into the FE model.

In this model, the workpiece is defined as an Eulerian domain whereas the tool was modeled as a Lagrangian domain. As an example of the FE discretization, Figure 1(a) shows the 3D Eulerian domain with a volume of $20\times20\times7$ mm³, which is meshed with 23,016 thermally coupled Eulerian elements (EC3D8RT) with an element size of 0.5 mm and having four degrees of freedom per node (displacement and temperature). The Eulerian domain is made up of two main regions: the blue part (material region) was assigned to the Aluminum alloy with a thickness of 6 mm and the red zone (empty region) with a thickness of 1 mm. While there is no material in the red zone in the reference configuration, this zone permits flash formation above the surface of the workpiece during welding.

The meshed tool and tool dimensions are presented in Figure 1(b). The tool is modeled as a Lagrangian rigid body with 23,522 4-node thermally coupled tetrahedron (C3D4T) elements with an element size of 0.6 mm. The simplified tool was oriented at a zero-tilt angle as a three-flat straight probe without threads using the average diameter of the experimental probe. The plunging and dwelling phases of the process were not modeled to minimize the computational time steps needed by the explicit solver, but instead, the simulation begins with the tool starting at an initial plunge depth. To ensure that there are no spurious numerical measurements from the initial few time steps when the tool is achieving mechanical equilibrium with the surrounding material of the workpiece, numerical results were only investigated after the tool reaction forces reached a steady-state condition.

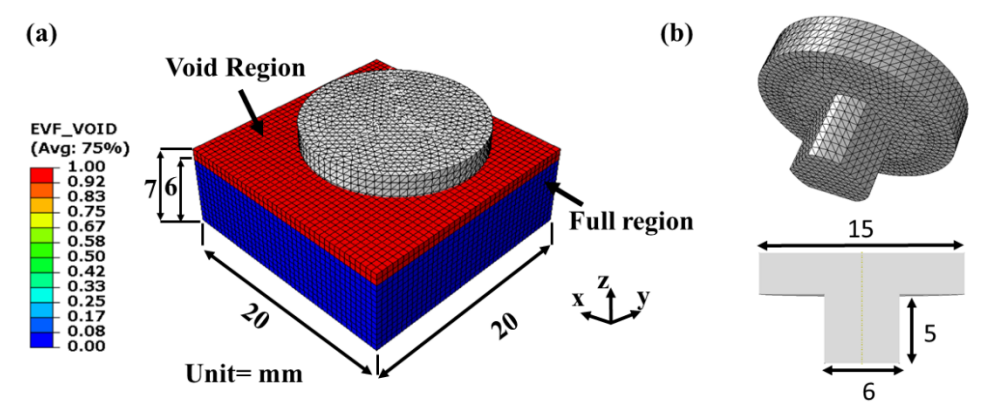


Figure 1. Numerical model geometry and its discretization (mesh) for (a) the workpiece domain, and (b) the tool.

All of the tool movements were assigned to the tool reference point to control the tool motion accurately. Tool runout was applied by offsetting the body of the tool from the tool reference point around which the tool rotated at 1000 rpm. The body was offset 32 µm to achieve the true runout of 64 µm that was measured in the experiment (Figure 2(b)) [31]. Elastic compliance of the setup was modeled by adding linear spring elements between the reference point of the tool and fixed points in the X, Y, and Z directions (Figure 2(a)). Since the tool eccentric motion occurs in the horizontal X-Y plane, the spring element in the Z direction was set to an infinite value to isolate the tool deflection in the welding plane. The X and Y direction spring stiffness are set to the predetermined values from the experiments (6150 kN/m and 8300 kN/m respectively). The welding phase is simulated by setting the inflow and outflow velocities of the domain equal to the travel speed of the process (Figure 2(b)). Zero material velocity constraints were applied on all the other exterior surfaces to prevent material from deforming out of the domain.

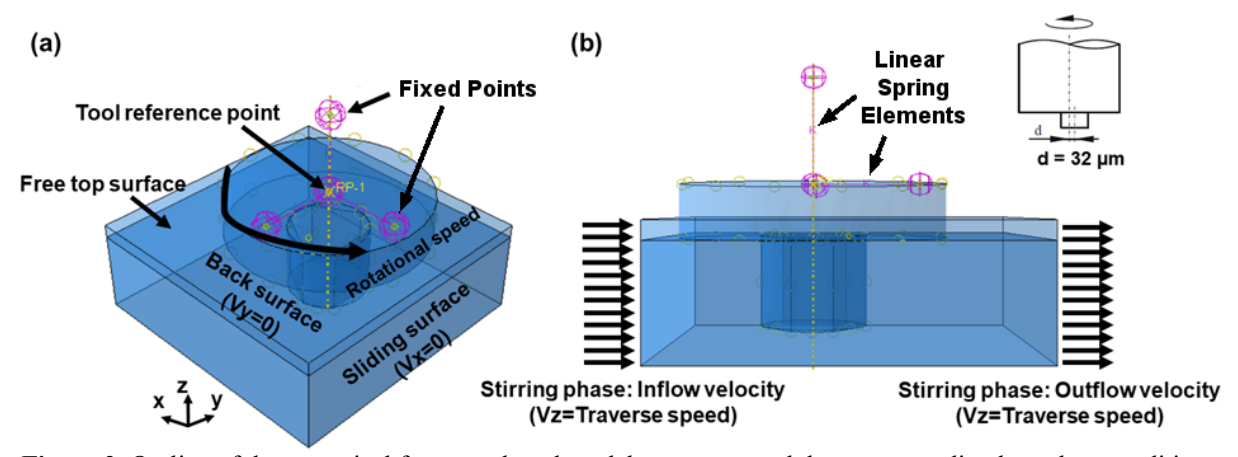


Figure 2. Outline of the numerical framework and model geometry, and the corresponding boundary conditions applied in the model.

3. Results and discussion

We now present the numerical simulation results and a discussion of the force dependence on various process parameters. To do so, we first discuss the graphical representation of the reaction forces on the tool in the polar coordinate system. This representation is ideally suited to compare the force magnitude variations as a function of the tool angle and as a function of the defect location and morphology in relation to the tool rotation.

3.1. Tool reaction forces represented as a polar plot of tool rotation.

The oscillatory reaction forces on the tool as it stirs the material around it are a result of the interactions of the near-rigid probe with the intermittent plastic flow of the material around the probe. Distortion of the oscillatory reaction forces during the formation of volumetric voids (material defects) needs a fundamental understanding of the process mechanisms that drive the plastic flow around the probe.

Since the rotating probe encounters different regimes of plastic flow as it moves between the advancing and retreating sides of the weld, we hypothesize that reaction forces (caused due to the interaction of the probe, particularly the leading edge of the probe with the surrounding material) can be used as an important signature to estimate the weld quality around the probe. Figure 3 shows the process coordinate system where the X force is acting on the probe surface normal to the welding direction, the Y force is acting along the welding direction, and the Z force is the vertical force acting on the tool. To plot the polar plot of the resultant force, an angular encoder was used to measure the tool angular position within the process, and this is described in our earlier publication [31]. The resultant force acting in the X-Y plane is the net effect of the forces applied by the material to the probe. It is important to note that, while the total force magnitude would also involve the Z component of the force, it is found that the magnitude of the radial in-plane forces is more useful in correlating with the occurrence of voids than the entire force magnitude.

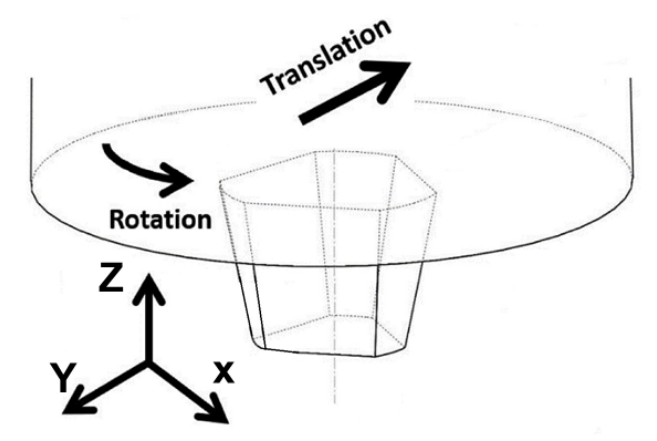


Figure 3. Assumed coordinate system to track the evolution of forces during the FSW process. The in-plane radial force magnitude $(F_r = \sqrt{F_X^2 + F_Y^2})$ is the relevant force metric considered in this study.

Figure 4 shows a polar plot of the resultant radial force for a full revolution of the tool with both voided (1000 rpm, 600 mm/min) and non-voided (1000 rpm, 200 mm/min) welds. For both cases, the plot is elongated along the welding direction. Further, for the voided case, there is a significant deviation (indicated by arrows) from the ellipsoidal shape observed in the non-voided case. These two cases already demonstrate that interesting variations to the reaction forces can be expected as a function of the travel direction and defect occurrence. We seek to expand on this observation and demonstrate the dependence of the force variations on different process parameters. The goal is to establish the in-plane radial force measure as an important metric for detecting voids, and thereby characterizing weld quality.

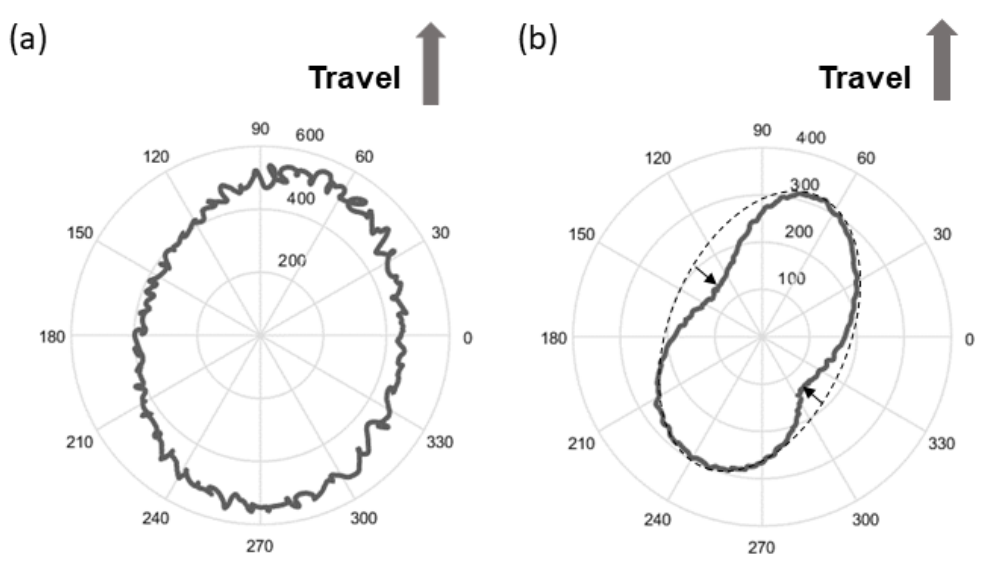


Figure 4. Polar plot of the in-plane radial force for one rotation of the tool for: (a) non-voided conditions, and (b) voided conditions.

3.2. Numerical studies

As part of the numerical studies, in addition to the force measurements, we track the evolution of void formation. To help with the visualization of void formation, a horizontal section (A-A) of the model is used to track the tool probe motion as shown in Figure 5. This cross-section is extracted from the numerical model after the process forces reach a near steady-state. This cross-section is used to understand the interaction of the probe with the surrounding material or volumetric voids within the weld. Within Abaqus, a view cut with a Eulerian volume fraction (EVF) of 0.5 is extracted as field output to obtain this cross-section and the possible void geometry inside.

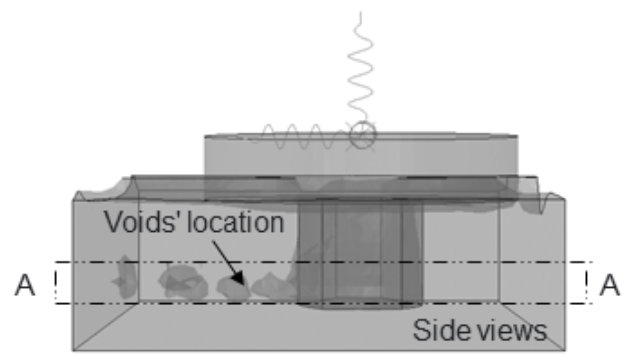


Figure 5. Section A-A chosen to track the formation and evolution of voids during the welding process

3.2.1. Validation study: Comparison of numerical and experimental force response

Before venturing into the estimation of numerical correlations between the forces and the underlying voids, we try to provide some validation of the numerical force measurements. Towards this goal, we experimentally measure the force signal in the X direction for one full rotation of the tool for a given welding condition (1000 rpm, 600 mm/min) and compared this with the numerically obtained value of this force component. The resulting comparison of the experimental and numerical forces values is shown in Figure 6. As can be seen, the overall force profiles (peak magnitudes and temporal evolution) match significantly. The finer differences in the force profiles are to be expected as the numerical model is

only an approximation of the experimental setup, and the tool stiffness, material properties, and process conditions are only closely approximated and not exactly represented as in any numerical model of this complexity. This comparison gives us confidence in the overall representation of the process conditions, rate and temperature dependent elasto-plastic material properties, and tool-workpiece interactions, and demonstrates the utility of the numerical model to simulate the physics of probe-void interaction and resulting void formation.

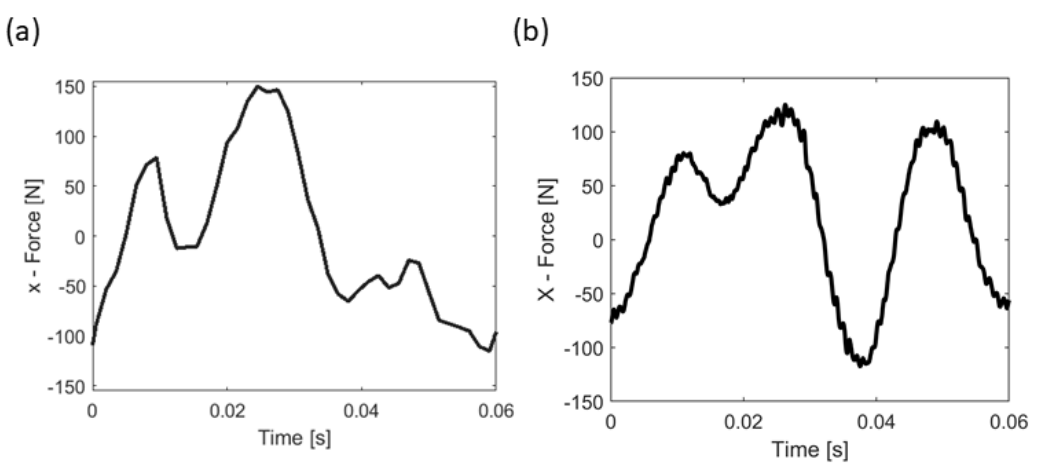


Figure 6. X-force signal for one tool revolution: (a) extracted from numerical simulation and (b) experimentally measured

3.2.2. Force variation as a function of probe-void interaction

The fundamental understanding of probe-void interaction causing force signal distortion is important for the development of force-based void detection. This study tries to explain probe-void interaction through an inspection of the radial force response, represented as a polar plot in the X-Y plane, in the case of voided and non-voided welds (Figure 7). Both voided (1000 rpm, 600 mm/min) and non-voided (1000 rpm, 200 mm/min) cases for the three-flat tool with no runout were considered. Because the tool does not have any eccentricity, each peak of the probe of the tool has a similar contact condition with the surrounding material. When there is no volumetric void, the peaks of the probe are in contact with the surrounding material during the entire rotation of the tool, resulting in a near circular force plot (Figure 7a). However, when there is void formation, due to excessive process conditions, the force plot shows three distinct regions of deviation from a circular force profile (Figure 7b). These regions are highlighted with arrows in Figure 7b. We attribute each of these three deviations in the force plot shape to the lack of interaction between each of the three peaks of the probe and the volumetric void in the surrounding material. When the peaks of the probe interact with the void, there is a drop in the force value, as the void offers reduced reaction to the probe due to the absence of material that needs to be stirred and forged.

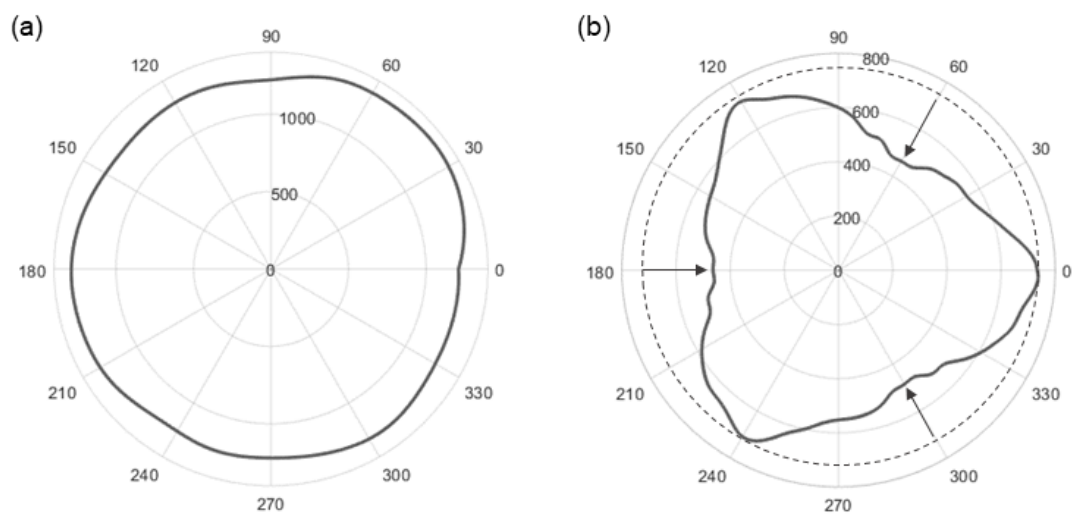


Figure 7. Polar plot of the radial force obtained from one rotation of the tool with no-runout for (a) good (non-void) welding condition and (b) voided welding condition

This correlation between the drop in the radial force value and the underlying void is clearly demonstrated in Figure 8 and Figure 9. In both figures, we show three different snapshots of the void location with respect to the probe and the corresponding radial force vector. While Figure 8 is the observation from a non-voiding case, Figure 9 is the observation from a voiding case. The near circular pattern of the force plot indicates consistent contact between the probe peaks and the surrounding material, without any significant force deviation that is characteristic of probe-void interaction. However, when a volumetric void is formed, the force plot shows significant deviation (indicated by arrows in the force plot in Figure 9) from a circular pattern at three distinct points. By comparison with the void location shown in the top row of Figure 9, we can confidently deduce that each of the three depressions in the force plot is due to the interactions of the three probe peaks with the void in their wake. Detailed videos, showing the probe-void interactions seen in the numerical simulations, can be found in the supplementary material.

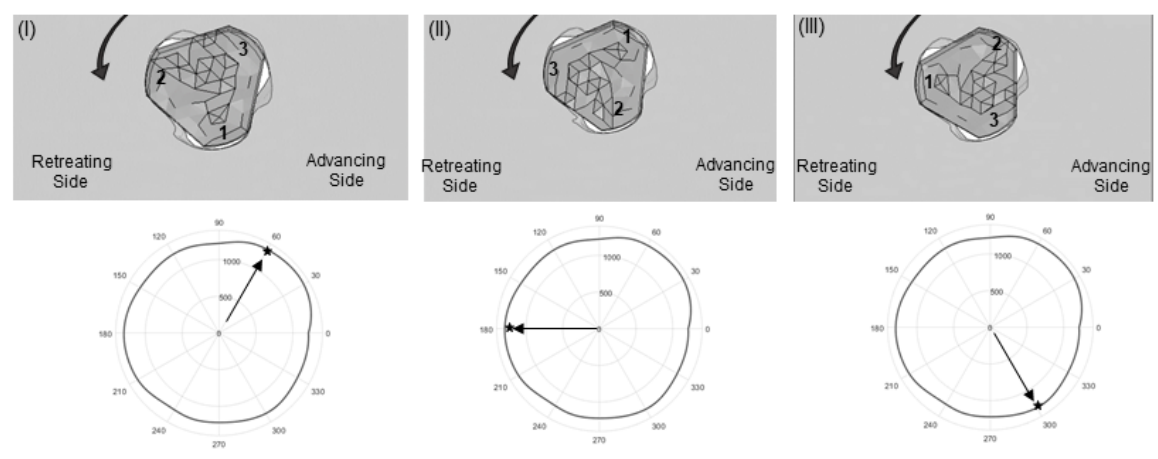


Figure 8. Interaction of the peaks of the probe with surrounding material for a non-voided case (top row) and the corresponding radial force plots (bottom row) shown at three different instances within a single rotation of the tool.

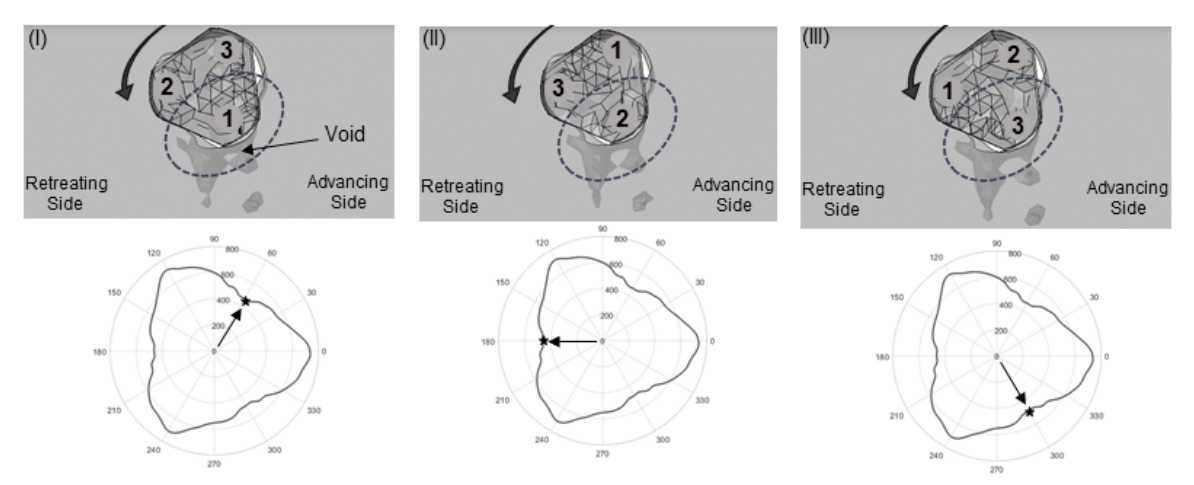


Figure 9. Interaction of the peaks of the probe with the surrounding material for a voided case (top row) and the corresponding radial force plots (bottom row) shown at three different instances within a single rotation of the tool. the void region is marked by the dotted ellipse.

This important correlation between the radial force and the corresponding interaction of the probe with the underlying void suggests that one could use the deviations in the radial force signal to identify potential void formation. Besides the detection of the void, the magnitude of the force deviation can also potentially indicate the void morphology (size and shape). More detailed correlations of the void morphology and force magnitudes will be addressed in a subsequent publication.

In addition to the above observations, we note that the tool profile, tool runout, and stiffness of the system are also very important to force-based void detection. For example, having a sharper probe peak causes more deflection of the probe into the volumetric void and creates a larger force plot depression. Additionally, tool runout makes one peak of the probe more eccentric than the other peaks. It changes the contact between peaks of the probe and the surrounding material that drives the plastic flow. Furthermore, a stiffer tool may not be as responsive, because it cannot easily deflect into the volumetric void. These effects of the tool runout and system stiffness will be examined in the following sections.

3.2.3. Force variation as a function of tool runout

Welds in the voided and non-voided process regimes were simulated with a 64 µm runout of the tool to examine the force variations and material flow around the probe. This condition produces the most eccentricity of the probe peak, and hence the contact conditions between each peak of the probe and the surrounding material will be different. Figure 10 shows the force plot for both the voided and non-voided welds with a tool runout. Clearly, the probe-void interaction is different than the earlier case with a norunout tool. In the non-voiding process condition, the peaks of the probe maintain full contact with the surrounding material during the entire rotation of the tool. This is the reason the force plot does not have any localized depressions (Figure 10a). Relative to this plot, the force plot for the voiding case has two distinct depressions in the force plot (shown with arrows in Figure 10b). Further, the overall shape also has significant variation from a circular shape. On closer examination (refer to videos of the simulation provided as Supplementary Material), this perturbation of the force plot and these two distinct regions of depression in the force magnitude occur due to the reduced contact between the probe and the surrounding material (due to the presence of a volumetric void), in addition to the perturbed motion of the tool caused due to the runout as compared to earlier cases. In comparison to the tool with no runout, the amplitude of the force plot for both the voided and non-voided welds is moderately stretched in the welding direction.

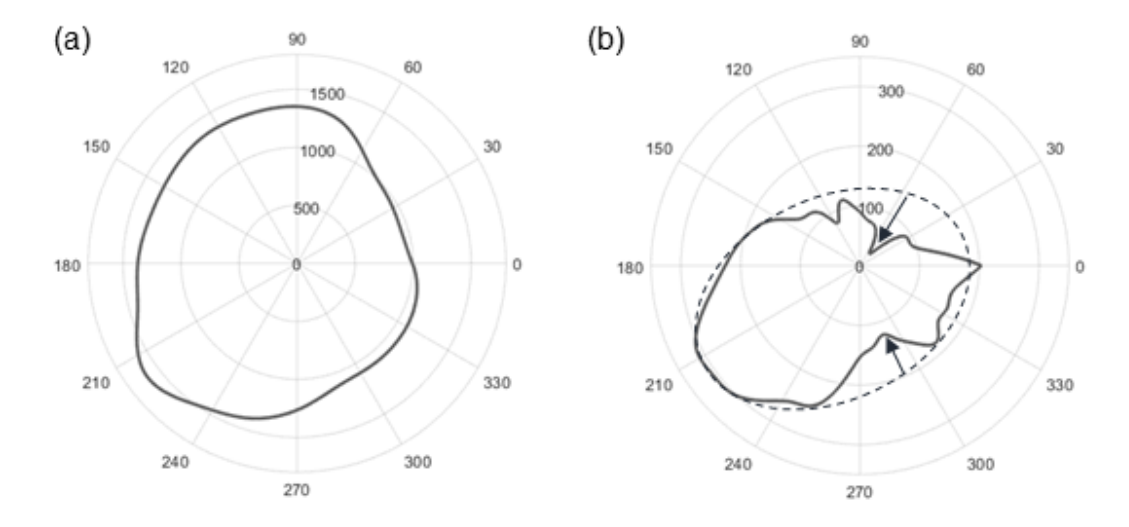


Figure 10. Polar plot of the radial force obtained from one rotation of the tool with runout for (a) non-void welding condition, and (b) voided welding condition

This correlation between the drop in the radial force value and the underlying void for this case is demonstrated in Figure 11. Subfigure 11(I) shows the instance when the most eccentric peak of the probe moves into the void on the retreating side of the weld. Because the tool is nominally deflected toward the advancing side of the weld due to the average process force in the X-direction [31], having a void in the retreating side causes relaxation of the loaded spring that in turn distorts the forces signals and produces a depression in the force plot. Subfigure 11(II) shows the second probe-void interaction. In this interaction, the most eccentric peak of the probe momentarily deflects towards the void in the advancing side of the weld due to the lack of the contact force that constrains the eccentric motion of the tool. These simulation results of the probe-void interaction for the case with runout show good agreement with the experimental force signals and tool deflections for this setup described in our earlier publication [31]. Detailed videos, showing the probe-void interactions seen in the numerical simulations, can be found in the supplementary material.

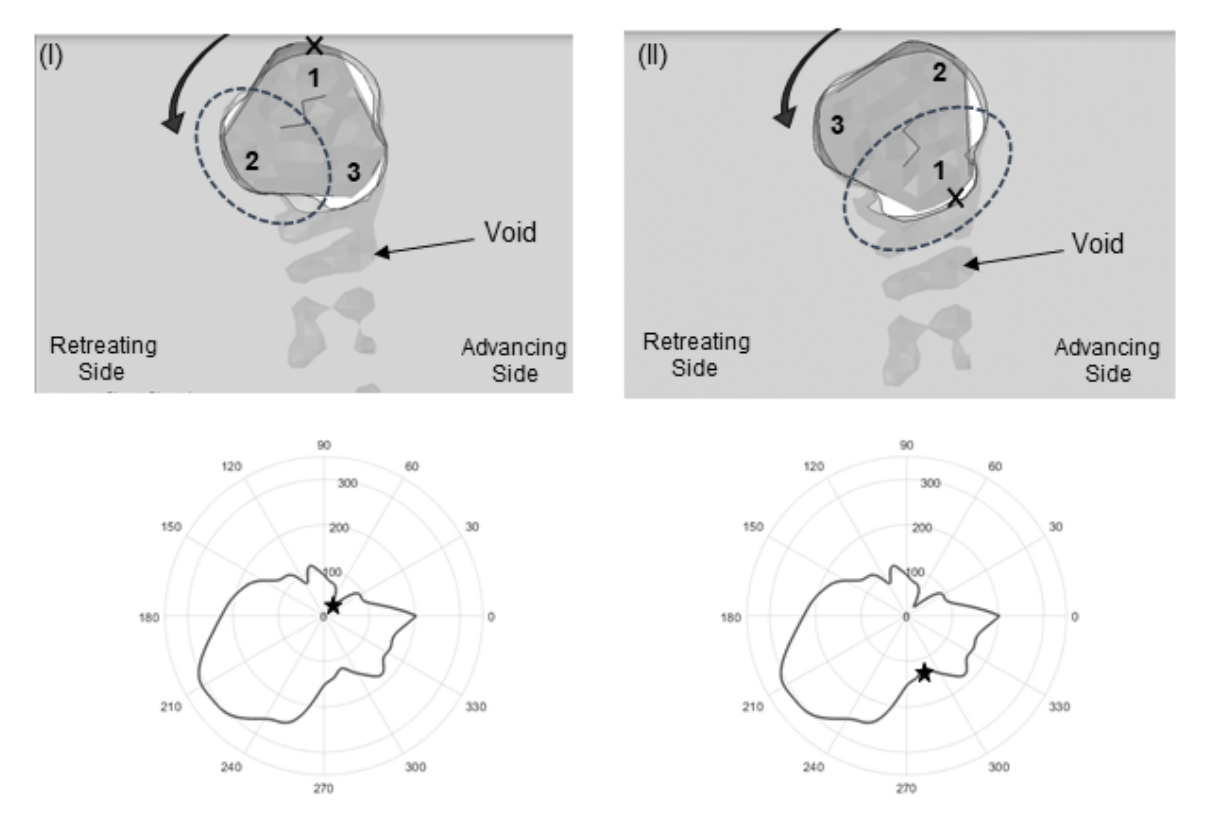


Figure 11. Interaction of the peaks of the probe with tool runout with the surrounding material for a voided case (top row) and the corresponding radial force plot (bottom row) shown at two different instances within a single rotation of the tool

3.2.4. Force variation as a function of the system elastic stiffness

In the previous sections, we mentioned that the tool probe can deflect into the volumetric void regions and produce perturbations in the force plot. This alludes to a potential role of the effective elastic stiffness of the overall setup as it affects the dynamic motion of the tool and its ability to swing away from the central axis of rotation. The stiffness of the setup results from the elastic stiffness of the milling machine plus the tool and the tool holder, as described in Section 2.1. Because the FSW machines that are used in industrial applications are stiffer than the milling machine based setup used in this work, it is important to model the effect of the elastic stiffness of the setup to see how a stiffer setup performs. In general, a stiffer setup may lead to reduced tool deflection into the volumetric void.

Accordingly, welds in a voiding scenario with no tool runout were simulated with two different stiffness setups. One with the stiffness of our experimental milling machine (referred to as the regular setup), and another with a stiffness that is 10⁶ higher than that of the regular setup to model a near rigid setup. Figure 12 shows the force plot for both the stiffness conditions. As the figure shows, like the regular setup (Figure 12a), the stiffer setup (Figure 12b) also shows three primary depressions in the force plot (indicated with arrows). However, the force magnitudes are much larger due to the increased stiffness (more force is needed to produce a given deflection of the tool), and the overall force profile is seen to have multiple perturbations from the relatively more smoother force profile for the regular setup. These simulations demonstrate that, in addition to the dependence of the force values on the setup stiffness, the methodology outlined in this paper to use force plots to detect voids is still reliable even in cases with near rigid FSW system setups that can be found in industrial applications.

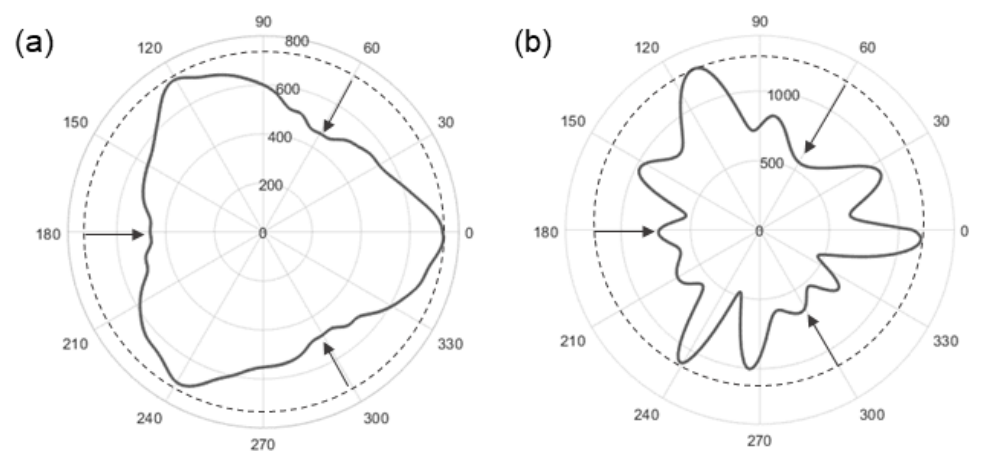


Figure 12. Polar plot of the in-plane force for a tool with no-runout for one tool rotation for (a) regular CNC milling machine stiffness, and (b) near-rigid setup with 10⁶ times of the milling machine stiffness.

4. Conclusions

In this work, we introduce polar plots of in-plane radial reaction forces on the tool as a strong candidate for in-situ detection of void formation. We consider different process conditions that produce non-voided and voided welds, and study the influence of probe-void interaction, tool runout, and system stiffness on the evolution of the reaction force profiles and their correlation with underlying void occurrence. In each case, we provide insights into the potential causes for perturbations in the force profile and relate important distinct variations of the force profile with the underlying probe-void interactions. In summary, the following conclusions can be drawn from this study:

- Experiments and simulations show a strong correlation between void formation and perturbations to the in-plane reaction forces on the tool. This is due to the tool probe deflecting into the void region that then reduces the effective contact between the peak of the probe and the surrounding material. This, in turn, reduces the process forces that appear as a distinct depression in the force plot.
- Comparing the cases of a tool without any runout and a tool with runout, we observe that the force plot changes from near circular to an elliptical shape due to a significant difference in the plastic flow of material around the tool probe. Specifically, tool runout changes the interaction between the probe peaks and the surrounding material, and instead of having three primary instances of probe-void interaction (as observed for a tool without runout), only two instances of probe-void interactions are observed. Hence, considering the effect of tool runout is important for in-situ force-based void monitoring.
- The effect of system stiffness on the probe-void interactions was also investigated. Results show that FSW setups with higher system stiffness are as sensitive as regular CNC milling machines based FSW setups for producing distinct perturbations and depressions in the radial force profile. However, for the higher stiffness setups, the force magnitudes are much larger, and the overall force profile is seen to have multiple perturbations as compared to the relatively smoother force profile of the regular setup.

5. Acknowledgments

The authors gratefully acknowledge the financial support for this work from the U.S. National Science Foundation (NSF Grant No. CMMI-1826104)., the department of Mechanical Engineering at the University of Wisconsin-Madison, and colleagues in the Multiscale Metal Manufacturing Processes Lab.

References:

- [1] Thomas, W.M., Nicholas, E.D., Needham, J.C., Murch, M.G., Temple-Smith, P. and Dawes, C.J., 1991, "Friction stir butt welding," international patent application no. PCT/GB92 Patent application, (9125978.8).
- [2] Leal, R.M. and Loureiro, A., 2004, "Defects formation in friction stir welding of aluminium alloys," Mater. Sci. Forum, 455, 299-302. https://doi.org/10.4028/www.scientific.net/MSF.455-456.299.
- [3] Mishra, R.S. and Ma, Z.Y., 2005, "Friction stir welding and processing," Mater. Sci. Eng. R, 50(1-2), pp.1-78. https://doi.org/10.1016/j.mser.2005.07.001.
- [4] Yoshikawa, K., 2003, "A joining criterion for lap joining of dissimilar metal materials of aluminum and stainless steel by friction stir," In The 4th International Symposium on Friction Stir Welding, Park City, Utah, USA, 14-16.
- [5] Arbegast, W.J., 2008, "A flow-partitioned deformation zone model for defect formation during friction stir welding," Scr. Mater., 58(5), pp.372-376. https://doi.org/10.1016/j.scriptamat.2007.10.031.
- [6] Boldsaikhan, E., Burford, D.A. and Gimenez, P., 2011, "Effect of plasticized material flow on the tool feedback forces during friction stir welding," In Proc. Conf. On 'Friction stir welding and processing VI', San Francisco, CA, USA, pp. 335-343.
- [7] Zaeh, M.F. and Gebhard, P., 2010, "Dynamical behaviour of machine tools during friction stir welding," J. Prod. Eng., 4(6), pp.615-624. https://doi.org/10.1007/s11740-010-0273-y.
- [8] Fonda, R., Reynolds, A., Feng, C.R., Knipling, K. and Rowenhorst, D., 2013, "Material flow in friction stir welds," Metall. Mater. Trans. A, 44(1), pp.337-344. https://doi.org/10.1007/s11661-012-1460-6.
- [9] Qian, J.W., Li, J.L., Xiong, J.T., Zhang, F.S., Li, W.Y. and Lin, X., 2012, "Periodic variation of torque and its relations to interfacial sticking and slipping during friction stir welding," Sci. Technol. Weld, 17(4), pp.338-341. https://doi.org/10.1179/1362171812Y.0000000001.
- [10] Reynolds, A.P., 2008, "Flow visualization and simulation in FSW," Scr. Mater., 58(5), pp.338-342. https://doi.org/10.1016/j.scriptamat.2007.10.048.
- [11] Nunes Jr, A.C., 2006, "Metal flow in friction stir welding," In Materials Science and Technology 2006/ASM International, The Minerals, Metals and Materials Society.
- [12] Chen, Z.W. and Cui, S., 2008, "On the forming mechanism of banded structures in aluminium alloy friction stir welds," Scr. Mater., 58(5), pp.417-420. https://doi.org/10.1016/j.scriptamat.2007.10.026.
- [13] Li, W.Y., Li, J.F., Zhang, Z.H., Gao, D.L. and Chao, Y.J., 2013, "Metal flow during friction stir welding of 7075-T651 aluminum alloy," Exp. Mech., 53(9), pp.1573-1582. https://doi.org/10.1007/s11340-013-9760-3.
- [14] Shrivastava, A., Zinn, M., Duffie, N.A., Ferrier, N.J., Smith, C.B., and Pfefferkorn, F.E., 2017, "Force measurement-based discontinuity detection during friction stir welding," J. Manuf. Process., 26, pp.113-121. https://doi.org/10.1016/j.jmapro.2017.01.007.
- [15] Mandache, C., Dubourg, L., Merati, A. and Jahazi, M., 2008, "Pulsed eddy current testing of friction stir welds," Mater. Eval., 66(4).
- [16] Tabatabaeipour, M., Hettler, J., Delrue, S. and Van Den Abeele, K., 2015, "Nondestructive ultrasonic inspection of friction stir welds," Phys. Procedia, 70, pp.660-663. https://doi.org/10.1016/j.phpro.2015.08.071.
- [17] Bird, C.R., 2004, "Ultrasonic phased array inspection technology for the evaluation of friction stir welds," Insight: Non-Destr. Test. Cond. Monit., 46(1), pp.31-36. https://doi.org/10.1784/insi.46.1.31.52658.
- [18] Mishra, D., Roy, R.B., Dutta, S., Pal, S.K. and Chakravarty, D., 2018, "A review on sensor based monitoring and control of friction stir welding process and a roadmap to Industry 4.0," J. Manuf. Process., 36, pp.373-397. https://doi.org/10.1016/j.jmapro.2018.10.016.
- [19] Jene, T., Dobmann, G., Wagner, G. and Eifler, D., 2008, "Monitoring of the friction stir welding process to describe parameter effects on joint quality," WELD WORLD, 52(9), pp.47-53. https://doi.org/10.1007/BF03266668.
- [20] Fleming, P., Lammlein, D., Wilkes, D., Fleming, K., Bloodworth, T., Cook, G., Strauss, A., DeLapp, D., Lienert, T., Bement, M. and Prater, T., 2008, "In-process gap detection in friction stir welding," Sens. Rev., 28; 62-67. https://doi.org/10.1108/02602280810850044.
- [21] Ramulu, P.J., Narayanan, R.G., Kailas, S.V. and Reddy, J., 2013, "Internal defect and process parameter analysis during friction stir welding of Al 6061 sheets," Int. J. Adv. Manuf. Technol., 65(9-12), pp.1515-1528. https://doi.org/10.1007/s00170-012-4276-z.
- [22] Kumari, S., Jain, R., Kumar, U., Yadav, I., Ranjan, N., Kumari, K., Kesharwani, R.K., Kumar, S., Pal, S., Pal, S.K. and Chakravarty, D., 2019, "Defect identification in friction stir welding using continuous wavelet transform," J. Intell. Manuf., 30(2), pp.483-494. https://doi.org/10.1007/s10845-016-1259-1.
- [23] Das, B., Pal, S. and Bag, S., 2016, "A combined wavelet packet and Hilbert-Huang transform for defect detection and modelling of weld strength in friction stir welding process," J. Manuf. Process., 22, pp.260-268. https://doi.org/10.1016/j.jmapro.2016.04.002.

- [24] Boldsaikhan, E., Corwin, E.M., Logar, A.M. and Arbegast, W.J., 2011, "The use of neural network and discrete Fourier transform for real-time evaluation of friction stir welding," Appl. Soft Comput., 11(8), pp.4839-4846. https://doi.org/10.1016/j.asoc.2011.06.017.
- [25] Schmidt, H. and Hattel, J., 2004, "A local model for the thermomechanical conditions in friction stir welding," Model. Simul. Mater. Sci. Eng., 13(1), p.77. https://doi.org/10.1088/0965-0393/13/1/006.
- [26] Al-Badour, F., Merah, N., Shuaib, A. and Bazoune, A., 2013, "Coupled Eulerian Lagrangian finite element modeling of friction stir welding processes," J. Mater. Process. Technol., 213(8), pp.1433-1439. https://doi.org/10.1016/j.jmatprotec.2013.02.014.
- [27] Zhu, Y., Chen, G., Chen, Q., Zhang, G. and Shi, Q., 2016, "Simulation of material plastic flow driven by non-uniform friction force during friction stir welding and related defect prediction," Mater. Des., 108, pp.400-410. https://doi.org/10.1016/j.matdes.2016.06.119.
- [28] Dialami, N., Cervera, M., Chiumenti, M. and Segatori, A., 2019, "Prediction of joint line remnant defect in friction stir welding," Int. J. Mech. Sci., 151, pp.61-69. https://doi.org/10.1016/j.ijmecsci.2018.11.012.
- [29] Dialami, N., Cervera, M. and Chiumenti, M., 2020, "Defect formation and material flow in friction stir welding," European Journal of Mechanics-A/Solids, 80, p.103912. https://doi.org/10.1016/j.euromechsol.2019.103912.
- [30] Ajri, A. and Shin, Y.C., 2017, "Investigation on the effects of process parameters on defect formation in friction stir welded samples via predictive numerical modeling and experiments," J. Manuf. Sci. Eng., 139(11). https://doi.org/10.1115/1.4037240
- [31] Franke, D., Rudraraju, S., Zinn, M. and Pfefferkorn, F.E., 2020, "Understanding process force transients with application towards defect detection during friction stir welding of aluminum alloys," J. Manuf. Process., 54, pp.251-261. https://doi.org/10.1016/j.jmapro.2020.03.003.
- [32] Abaqus, F.E.A., 2017. Dassault Systemes Simulia Corporation. Providence, Rhode Island, USA.
- [33] Ansari, M.A., Franke, D., Zinn, M., Pfefferkorn F.E., and Rudraraju S., "Predictive modeling of defect formation and material flow in Friction Stir Welding of Aluminum Alloys," (under review).

Figure Caption List

Figure 1	Numerical model geometry and its discretization (mesh) for (a) the workpiece domain, and (b) the tool
Figure 2	Outline of the numerical framework and model geometry, and the corresponding boundary conditions applied in the model
Figure 3	Assumed coordinate system to track the evolution of forces during the FSW process. The in-plane radial force magnitude $(F_r = \sqrt{F_X^2 + F_Y^2})$ is the relevant force metric considered in this study
Figure 4	Polar plot of the in-plane radial force for one rotation of the tool for: (a) non-voided conditions, and (b) voided conditions
Figure 5	Section A-A chosen to track the formation and evolution of voids during the welding process
Figure 6	X-force signal for one tool revolution: (a) extracted from numerical simulation and (b) experimentally measured
Figure 7	Polar plot of the radial force obtained from one rotation of the tool with no-runout for (a) good (non-void) welding condition and (b) voided welding condition
Figure 8	Interaction of the peaks of the probe with surrounding material for a non-voided case (top row) and the corresponding radial force plots (bottom row) shown at three different instances within a single rotation of the tool
Figure 9	Interaction of the peaks of the probe with the surrounding material for a voided case (top row) and the corresponding radial force plots (bottom row) shown at three different instances within a single rotation of the tool. the void region is marked by the dotted ellipse
Figure 10	Polar plot of the radial force obtained from one rotation of the tool with runout for (a) non-void welding condition, and (b) voided welding condition
Figure 11	Interaction of the peaks of the probe with tool runout with the surrounding material for a voided case (top row) and the corresponding radial force plot (bottom row) shown at two different instances within a single rotation of the tool
Figure 12	Polar plot of the in plane force for a tool with no-runout for one tool rotation for (a) regular CNC milling machine stiffness, and (b) near-rigid setup with $[10]$ ^6 times of the milling machine stiffness

Table Caption List

Table 1 Experimental details